



## Emission factors and evolution of SO<sub>2</sub> measured from biomass burning in wild and agricultural fires

Pamela S. Rickly<sup>1,2</sup>, Hongyu Guo<sup>1,3</sup>, Pedro Campuzano-Jost<sup>1,3</sup>, Jose L. Jimenez<sup>1,3</sup>, Glenn M. Wolfe<sup>4</sup>, Ryan Bennett<sup>5</sup>, Ilann Bourgeois<sup>1,2</sup>, John D. Crouse<sup>6</sup>, Jack E. Dibb<sup>7</sup>, Joshua P. DiGangi<sup>8</sup>, Glenn S. Diskin<sup>8</sup>, Maximilian Dollner<sup>9</sup>, Emily M. Gargulinski<sup>16</sup>, Samuel R. Hall<sup>10</sup>, Hannah S. Halliday<sup>11</sup>, Thomas F. Hanisco<sup>4</sup>, Reem A. Hannun<sup>4,12</sup>, Jin Liao<sup>4,13</sup>, Richard Moore<sup>8</sup>, Benjamin A. Nault<sup>14</sup>, John B. Nowak<sup>8</sup>, Claire E. Robinson<sup>8,15</sup>, Thomas Ryerson<sup>2,a</sup>, Kevin J. Sanchez<sup>8</sup>, Manuel Schöberl<sup>9</sup>, Amber J. Soja<sup>8,16</sup>, Jason M. St. Clair<sup>4,12</sup>, Kenneth L. Thornhill<sup>8</sup>, Kirk Ullmann<sup>10</sup>, Paul O. Wennberg<sup>6,17</sup>, Bernadett Weinzierl<sup>9</sup>, Elizabeth B. Wiggins<sup>8</sup>, Edward L. Winstead<sup>8</sup>, and Andrew W. Rollins<sup>2</sup>

<sup>1</sup>Cooperative Institute for Research in Environmental Science, University of Colorado, Boulder, CO, USA

<sup>2</sup>Chemical Sciences Laboratory, NOAA, Boulder, CO, USA

<sup>3</sup>Department of Chemistry, University of Colorado, Boulder, CO, USA

<sup>4</sup>Atmospheric Chemistry and Dynamics Lab, NASA Goddard Space Flight Center, Greenbelt, MD, USA

<sup>5</sup>Bay Area Environmental Research Institute, NASA Ames Research Center, Moffett Field, CA

<sup>6</sup>Division of Geological and Planetary Sciences, California Institute of Technology, Pasadena, CA, USA

<sup>7</sup>Earth System Research Center, University of New Hampshire, Durham, NH, USA

<sup>8</sup>NASA Langley Research Center, Hampton, VA, USA

<sup>9</sup>Faculty of Physics, Aerosol Physics and Environmental Physics, University of Vienna, 1090 Vienna, Austria

<sup>10</sup>Atmospheric Chemistry Observations and Modeling Laboratory, National Center for Atmospheric Research, Boulder, CO, USA

<sup>11</sup>Environmental Protection Agency, Research Triangle, NC, USA

<sup>12</sup>Joint Center for Earth Systems Technology, University of Maryland Baltimore County, Baltimore, MD 21250, USA

<sup>13</sup>Goddard Earth Science Technology and Research (GESTAR) II, University of Maryland Baltimore County, Baltimore, MD, USA



45 <sup>14</sup>CACC, Aerodyne Research, Inc.

<sup>15</sup>Science Systems and Applications, Inc., Hampton, VA, USA

50 <sup>16</sup>National Institute of Aerospace, Resident at NASA Langley Research Center, Hampton, VA, USA

<sup>17</sup>Division of Engineering and Applied Science, California Institute of Technology, Pasadena, CA, USA

<sup>a</sup>now at: Scientific Aviation, Boulder, CO, USA

*Correspondence to:* Pamela S. Rickly (pamela.rickly@noaa.gov)

55

**Abstract.** Fires emit sufficient sulfur to affect local and regional air quality and climate. This study analyzes SO<sub>2</sub> emission factors and variability in smoke plumes from US wild and agricultural fires, and their relationship to sulfate and hydroxymethanesulfonate (HMS) formation. Observed SO<sub>2</sub> emission factors for various fuel types show good agreement with the latest reviews of biomass burning emission factors, producing an emission factor range of 0.47 – 1.2 g SO<sub>2</sub> kg<sup>-1</sup> C in the emissions. These emission factors vary with geographic location in a way that suggests that deposition of coal burning emissions and application of sulfur-containing fertilizers likely play a role in the larger observed values, which are primarily associated with agricultural burning. A 0-D box model generally reproduces the observed trends of SO<sub>2</sub> and total sulfate (inorganic + organic) in aging wildfire plumes. In many cases, modeled HMS is consistent with the observed organosulfur concentrations. However, a comparison of observed organosulfur and modeled HMS suggests that multiple organosulfur compounds are likely responsible for the observations, but that the chemistry of these compounds yield similar production and loss rates to that of HMS, resulting in good agreement with the modeled results. We provide suggestions for constraining the organosulfur compounds observed during these flights and we show that the chemistry of HMS can allow for organosulfur to act as a S(IV) reservoir under conditions of increased pH (>6) and liquid water content (> 10<sup>-7</sup> g m<sup>-3</sup>). This can facilitate long-range transport of sulfur emissions resulting in increased SO<sub>2</sub> and eventually sulfate in transported smoke.

75

## 1 Introduction

Sulfate is a major component of PM<sub>2.5</sub>, contributing significantly to adverse air quality and severe haze events (Chan and Yao, 2008). A severe haze event in Beijing, China showed PM<sub>2.5</sub> sulfur concentrations reaching 100 µg/m<sup>3</sup> with aerosol optical depths over 1 (Moch et al., 2018). Sulfate aerosols are produced through the oxidation of sulfur dioxide (SO<sub>2</sub>) which was estimated to have a global emission rate of approximately 113 Tg S yr<sup>-1</sup> in 2014 (Hoesly et al., 2018). Approximately 67% of global SO<sub>2</sub> emissions are due to anthropogenic sources, primarily fossil fuel combustion and smelting (Lee et al., 2011; Smith et al., 2011; Feinberg et al., 2019).

85 While biomass burning is expected to contribute a smaller portion to global sulfur emissions (1.22 Tg S yr<sup>-1</sup>), the effects of climate change and land use change are expected to increase biomass burning events in both frequency and duration (Westerling et al., 2006;



Heyerdahl et al., 2002; Lee et al., 2011). Biomass burning SO<sub>2</sub> emissions can influence air quality through sulfate aerosol production in regions thousands of kilometers away from the burn site due to meteorological long-range transport (Fiedler et al., 2011). In extreme cases, pyrocumulonimbus formation injects biomass burning aerosol – including sulfate – into the upper troposphere and lower stratosphere (Fromm et al., 2005).

90  
Biomass burning produces both primary and secondary aerosols, with sulfate aerosols mostly from secondary production, but also a smaller primary component in some cases (Lewis et al., 2009). The chemical composition of aerosols produced during biomass burning is highly dependent on the environmental conditions and type of combustion occurring, flaming or smoldering. For example, elemental carbon and NO<sub>x</sub> are mainly emitted during the flaming stage, while emissions of VOCs and (mainly organic) PM<sub>2.5</sub> are larger during the smoldering phase (Pandis et al., 1995; Lobert et al., 1991; Burling et al., 2010). Fuel composition also influences SO<sub>2</sub> emissions. This is demonstrated in a recently published compilation of biomass burning emission factors utilizing only data from young smoke to limit conversion during chemical aging, reducing the variability within the published measurements (Andreae, 2019). This compilation shows savanna and grassland SO<sub>2</sub> emission factors to be  $0.47 \pm 0.44$  g SO<sub>2</sub> kg<sup>-1</sup> C and agricultural residues to be  $0.80 \pm 0.71$  g SO<sub>2</sub> kg<sup>-1</sup> C with a full fuel type range of 0.2 to 0.87 g SO<sub>2</sub> kg<sup>-1</sup> C.

105  
Oxidation of SO<sub>2</sub> in both the gas and aqueous phase produces sulfate, with a typical SO<sub>2</sub> lifetime of 0.6 – 2.6 days (Pham et al., 1995; Koch et al., 1999). However, the importance of some conversion mechanisms of SO<sub>2</sub> to sulfate remains poorly understood, resulting in the frequent underprediction of sulfate concentrations in atmospheric models by up to a factor of two for regional models (Wang et al., 2016; Shao et al., 2019; Wang et al., 2014). This underprediction has been reported for industrialized pollution where limited photochemistry is observed as a result of aerosol dimming (Cheng et al., 2016; Shao et al., 2019). While no known studies have reported on the modeling of SO<sub>2</sub> and sulfate chemistry in biomass burning smoke plumes, it is possible that similar phenomenon could occur because biomass burning plumes can have very high aerosol loading and thus dimming. However, the chemistry is likely to be different as a result of differing emissions. In addition, it has been suggested that unaccounted-for hydroxymethanesulfonate (HMS) formation may explain the discrepancy between measured and modeled sulfate values (Dovrou et al., 2019; Song et al., 2021).

115  
In this study, we quantify SO<sub>2</sub> emissions and examine the production of sulfate using airborne observations within a variety of smoke plumes. These measurements provide insight into the variable emission factors observed during biomass burning and allow for a comprehensive analysis of the conversion of SO<sub>2</sub> to sulfate and HMS including both gas- and aqueous-phase conditions. Smoke is a highly dynamic environment, and we examine how S chemistry is affected by radiation attenuation, enhanced aerosol liquid water content (LWC), and variable pH.

## 125 2 Methods

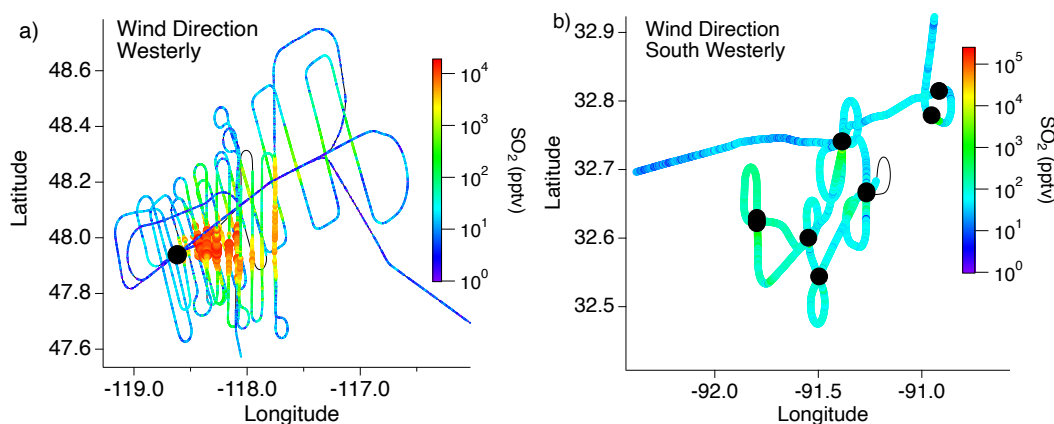
### 130 2.1 Mission and measurements

FIREX-AQ was a joint NASA-NOAA mission to study multiple aspects of fire emissions, chemistry, and impacts. Here we utilize observations from the NASA DC-8. The base locations for this aircraft campaign were Boise, ID from 21 July to 17 August and Salina, KS from 18



135 August to 5 September, 2019. The Boise, ID location allowed for the measurement of western U.S. wildfires, with sampling occurring in the late afternoon through evening. Salina-based flights focused on prescribed burns, primarily of croplands, within the midwestern and southern regions of the U.S. with measurements typically occurring in the afternoon. A subset of these measurements including seven different fuel types from over 80 fires is reported here.

140 Flight paths differed between the wildfire and cropland measurements. A typical flight path through the wildfire smoke plumes consisted of two “lawnmower” patterned passes consisting of about 10 staggered downwind transects perpendicular to the plume (Fig. 1). The closest transects were generally 10-15 km downwind due to flight restrictions, with the pattern extending as far as 200 km downwind resulting in smoke ages (based on Lagrangian trajectory analysis) ranging from 10’s of minutes to several hours. In contrast, sampling of smaller  
145 agricultural fires typically involved 1-2 plume intersections per fire.



150 *Figure 1. Typical flight path through (a) wildfire and (b) agricultural fire smoke plumes with the color and size of the markers indicating the SO<sub>2</sub> mixing ratio and the black markers indicating the fire locations.*

In situ measurements of SO<sub>2</sub> were performed using laser induced fluorescence (LIF SO<sub>2</sub>) in which SO<sub>2</sub> was excited at 216.9 nm by a custom-built fiber laser system with the red-shifted fluorescence detected between 240 and 400 nm. An intercomparison performed between the LIF  
155 SO<sub>2</sub> and Caltech CIMS instrument during FIREX-AQ showed good agreement between the two measurement techniques (Rickly et al., 2021). The accuracy of the LIF SO<sub>2</sub> measurements is ±9% + 2pptv, primarily dictated by uncertainty in the calibration standard concentration and spectroscopic background.

Sulfate measurements were performed with an Aerodyne high-resolution time-of-flight aerosol mass spectrometer (AMS) (DeCarlo et al., 2006; Canagaratna et al., 2007). This measurement technique allows for the speciation of submicron non-refractory particulate mass and the direct separation of inorganic and organic species having the same nominal mass to charge ratio (DeCarlo et al., 2006; Canagaratna et al., 2007). The standard AMS data analysis software reports both inorganic and organic sulfate as total sulfate, complicating the  
165 quantification of both types of sulfates (Farmer et al., 2010). While in the case of AMS total nitrate techniques for rapid assignment of organic nitrate based on its fragmentation pattern have been successfully developed (Fry et al., 2013; Day et al., 2021), the sulfate fragmentation pattern



is much more variable and hence similar approaches have so far had mixed success, depending on the aerosol characteristics (see Schueneman et al., 2021 for a review). In this work, we found the ion fragmentation method to produce reasonable results, based on the consistency with the results using positive matrix factorization (PMF, Paatero et al., 1994, Ulbrich et al., 2009) and the inorganic sulfate speciation provided by the SAGA instrument. As an additional constraint, the AMS apportionment can be compared with ion chromatography measurements reported by the SAGA instrument (Dibb et al., 2002; Heim et al., 2020), which quantifies only inorganic sulfate. The correlation between the AMS apportionment and SAGA measurements of inorganic sulfate shows an overall good agreement (Fig. S8). However, as discussed in section 4.2.2, for certain types of organosulfur compounds, hydrolysis in the liquid phase after capture into the instrument and before analysis might lead to SAGA detecting these as well, hence the SAGA sulfate measurements can be considered an upper limit on inorganic sulfate under FIREX conditions.

In situ CO concentrations were measured via wavelength modulation spectroscopy (Sachse et al., 1991), with an uncertainty of 2-7% over the dynamic range of the measurements. In situ CO<sub>2</sub> concentrations were measured using non-dispersive infrared spectrometry using a modified commercial spectrometer (Model 7000, LI-COR) similar to Vay et al., (2009), with uncertainties varying between 0.25 ppm and 2% of the measurements (whichever is larger) over the range of the measurements.

### 2.3 Emission factor calculation

Emission factors (EF) are defined as the mass of compound X relative to the mass of fuel burned; however, this can be substituted with the mass balance method which approximates the fuel mass by the sum of emitted carbon (Andreae, 2019). In accordance, the emission factors for SO<sub>2</sub> and sulfate were calculated as the enhancement ratio of each compound relative to the enhancement ratio of total carbon emitted per fire in units of g kg<sup>-1</sup> (Eq. 3.1). Because CO and CO<sub>2</sub> comprise approximately 95% of total carbon emissions, the summation of these values was used to represent total carbon.

$$EF(X) = \frac{X}{CO+CO_2} \cdot \frac{MM_X}{MM_C} \cdot F_C \cdot 1000 \quad (3.1)$$

The orthogonal distance regression slope of compound X to total carbon ( $\frac{X}{CO+CO_2}$ ) was determined for each transect through the smoke plume with a smoke age <1 hr to limit the influence of chemical processing due to atmospheric aging. Only emission ratio values with R<sup>2</sup> > 0.5 were included in the EF analysis. It is shown in sections 3.3 and 3.7 that no significant aging of SO<sub>2</sub> occurs within this length of time. In addition, only measurements ≥ 25% enhanced from the background were used, which allowed for the background mixing ratios to be neglected. MM<sub>X</sub> and MM<sub>C</sub> represent the molar mass of compound X and the summation of CO and CO<sub>2</sub>, respectively. The approximated value of 45% is used to represent the carbon fraction (F<sub>C</sub>) of the fuel emitted during these biomass burning events as outlined by Susott et al. (1996) and allows for a more direct comparison to the compilation of EF data prepared by Andreae (2019).

### 2.4 Modified combustion efficiency



215 The modified combustion efficiency (MCE) is a metric for combustion stage. The MCE is defined as the enhancement of CO<sub>2</sub> from the background in relation to the summation of the enhanced CO and CO<sub>2</sub> mixing ratios (Eq. 3.2). Traditionally, MCE > 0.9 is indicative of the flaming stage and an MCE < 0.9 is representative of the smoldering stage (Ferek et al., 1998; Sinha et al., 2003; Zhang et al. 2018). In reality, smoke sampled from large wildfires likely reflects a combination of variable fractions of flaming and smoldering combustion.

220

$$MCE = \frac{CO_2}{CO+CO_2} \quad (3.2)$$

## 2.5 Box Model

225 The Framework for 0-D Atmospheric Modeling (F0AM) was used to evaluate the evolution of SO<sub>2</sub> downwind of the fire location (Wolfe et al., 2016). Within F0AM, the Master Chemical Mechanism (MCM) version 3.3.1 was used to describe the evolution and chemistry of the gas-phase SO<sub>2</sub> and oxidant species. An additional mechanism describing the conversion of SO<sub>2</sub> to sulfate was implemented to address aerosol oxidation processes of sulfur compounds based on an establishment of equilibrium of the S(IV) compounds and oxidant species with relation to pH (Tang et al., 2014; D'Ambro et al., 2016; Seinfeld and Pandis, 2006). A complete list of the aqueous phase reactions and measurements used for model input is included in Tables S1-2 and the mechanism code is provided in the Supplementary Section 2.

235 The model was implemented to investigate the chemistry that occurred during the Williams Flats fire which was started 2 August 2019 through lightning ignition of timber/slash fuels in Keller, WA. Two separate flight days, 3 and 7 August, were modeled here using measurements acquired by the DC-8 in which two passes of lawnmower pattern paths were completed. These flights were analyzed by applying a Lagrangian model approach. The measurements were corrected for dilution by normalizing to CO (Müller et al., 2016) as follows:

240

$$\Delta_{dil}X = \frac{(X-X_b)}{(CO-CO_b)} \cdot CO_i \quad (3.3)$$

245 in which  $\frac{X}{CO}$  represents the ratio of compound X at each transect with respect to CO, X<sub>b</sub> and CO<sub>b</sub> are the background concentrations, and CO<sub>i</sub> represents the carbon monoxide mixing ratio at the source of the fire determined from the extrapolation of the transect average CO values. This extrapolation method was also applied to the dilution-normalized mixing ratios in order to initialize the model back to the fire source (t=0). The model was constrained to these initial concentrations, then allowed to run freely through the remainder of the flight time. The dilution rate was determined by matching the modeled CO to the measured CO decay using a Gaussian fit. However, CO<sub>i</sub>, used to determine the dilution normalized mixing ratio values, was based on the extrapolated CO initial value based on all transect CO values (core and edge).

250 Measurements were acquired through aircraft smoke plume penetration, which provided pseudo-Lagrangian observations by not entirely following the same air parcel. Comparison to a Lagrangian simulation is challenging because the aircraft measured different parts of the plume (core vs edge) and at different emission times. As a result, an exponential fit applied to the SO<sub>2</sub> and sulfate dilution-normalized mixing ratios against plume age is used to represent the measurement trend for comparison to the model results. While the model is not expected to



precisely reproduce the measurements based on plume age, due to variations in altitude between transects and subsequently varied pressures and temperatures, it does allow for the comparison of the overall trends of SO<sub>2</sub> and sulfate downwind of the source using averaged meteorological constraints.

Uptake of SO<sub>2</sub> and the oxidant species (O<sub>3</sub>, NO<sub>2</sub>, H<sub>2</sub>O<sub>2</sub>, and HCHO) to aerosol was represented within the model mechanism as a first-order loss (Seinfeld and Pandis, 2006):

$$k_{het} = 0.25 \cdot \gamma \cdot c \cdot v \quad (3.4)$$

where  $\gamma$  represents the uptake coefficient,  $c$  is the mean molecular speed of SO<sub>2</sub>, and  $v$  is the aerosol surface area based on average particle size distributions measured by a Laser Aerosol Spectrometer 3340. To account for the gas-phase diffusion limitation,  $\gamma$  was calculated by the following equation:

$$\gamma = \frac{1}{\alpha} + \frac{0.75 + 0.286Kn^{-1}}{Kn \cdot (Kn + 1)} \quad (3.5)$$

where  $\alpha$  represents the mass accommodation coefficient and  $Kn$  is the Knudsen number. Mass accommodation and gas diffusion coefficients used for deriving  $Kn$  and  $\gamma$  are listed in Table S3.

To represent equilibrium partitioning between the gas and aqueous phases, rates of condensation and evaporation were applied as described by D'Ambro et al. (2016):

$$k_{cond} = k_{het} \quad (3.6)$$

$$k_{evap} = \frac{k_{het}}{H \cdot LWC} \quad (3.7)$$

where  $H$  represents the Henry's Law constant of the species being adsorbed and  $LWC$  is the liquid water content of the cloud or aerosol. Because S(IV) production is pH dependent, individual equilibrium constants in relation to the H<sup>+</sup> produced by each reaction are required as an additional factor in the  $k_{evap}$  denominator as described by Seinfeld and Pandis (2006). As a result, the model accurately reproduces the S(IV) pH dependence (Fig. S1a) in which HSO<sub>3</sub><sup>-</sup> is the dominant form between the pH range of 2-7 and SO<sub>3</sub><sup>2-</sup> becomes the dominant form at pH > 7. Table S1 lists all aqueous phase reactions.

The rate of S(IV) oxidation exhibits a pH dependence based on the available oxidant species (Table S1) (Cheng et al., 2016). Using our model and the initial conditions from Guo et al. (2017), we reproduced very similar pH dependent oxidation rates to those shown in that study. However, initializing the model with the higher concentrations observed during FIREX-AQ increases the rates of oxidation as shown in Fig. S1b. This results in S(IV) oxidation being dominated by reaction with hydrogen peroxide at pH values < 5 which is within the range that aerosol sulfate production most commonly occurs in the U.S. For pH values approaching 5, there may be some competition amongst H<sub>2</sub>O<sub>2</sub>, O<sub>3</sub>, and HCHO depending on the oxidant concentrations. As pH values increase above 5, O<sub>3</sub>, NO<sub>2</sub>, and HCHO become the dominant oxidants with H<sub>2</sub>O<sub>2</sub> and NO<sub>2</sub> oxidation declining rapidly. Although the reaction of HCHO with S(IV) results in HMS production rather than inorganic sulfate, it has been included here to demonstrate its role in S(IV) oxidation. HCHO oxidation follows a very similar trend to O<sub>3</sub> oxidation, becoming a major S(IV) oxidant at higher pH. Further discussion of the HMS reactions listed in Table S1 can be found in the supplement.



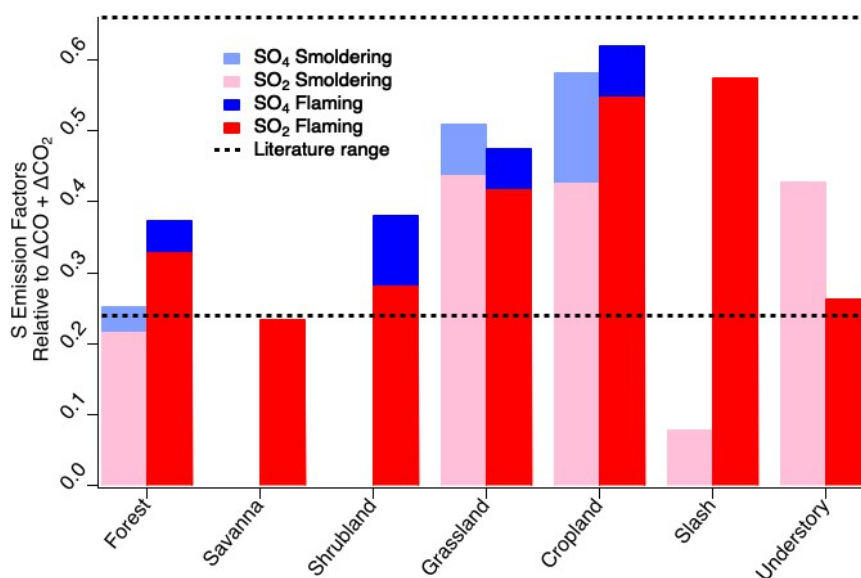
300 In this study, aerosol LWC and pH were determined via ISORROPIA-II thermodynamic  
modeling (Fountoukis and Nenes, 2007) in forward mode based on the AMS measured aerosol  
composition ( $\text{SO}_4$ ,  $\text{NO}_3$ ,  $\text{NH}_4$ , Cl) and collocated gas-phase measurements of  $\text{NH}_3$  and  $\text{HNO}_3$   
from PTR-MS and CIMS, respectively.  $\text{NH}_3$ - $\text{NH}_4$  is the most important species pair for  
constraining pH because it was not completely in either the gas or particle phase in the fire  
plumes or the background air mass. To improve the accuracy in thermodynamic modeling  
305 predictions, we removed the outliers when the predicted particle phase fraction of the  $\text{NH}_3$ - $\text{NH}_4$   
partitioning is off by more than 40% compared to the observation. Because these calculations are  
based on the inorganic aerosol concentrations, the LWC could potentially be up to several times  
greater due to the dominant organic portion in the fire plumes despite the lower hygroscopicity  
compared to the inorganics (Kreidenweis et al., 2008; Guo et al, 2015; Brock et al, 2016). The  
310 mixing state of inorganic and organic for the particles in the early phase plumes remains to be  
investigated but is likely to be phase separated given the low oxidation state of the organics  
(Sullivan et al., 2020). The current modeling can be interpreted as assuming a phase separation  
of inorganic vs. organics, with the chemistry studied occurring only in the inorganic-dominated  
phase and its associated water, with no kinetic limitations due to a potential core/shell or micelle  
315 like structures present in the particles. Due to the dominant organic fraction of sulfate signals in  
the fire plumes investigated in this study, addition bias and uncertainty derive from using the  
total AMS  $\text{SO}_4$  signals and zero non-volatile cations (e.g. not accounting for the potential  
contribution of soluble ions from ash, Adachi et al, 2022) in estimating LWC and pH. This is of  
particular concern when the uncertainties are larger than the estimated free acidity based on ion  
320 balance, as often happens near the neutralization point.

Most importantly, the modeling work presented in this study assumes an ideal solution.  
Given the relatively high ionic strength conditions observed for the 3 Aug ( $89.5 \pm 19.3$  M) and 7  
Aug ( $83.2 \pm 25.3$  M) flights due to the overall rather low RH, this can potentially lead to high  
deviations in the actual gas uptake coefficients, aqueous phase rate coefficients and to a lesser  
325 extent, pH (calculation of which does account for ionic strength, but is fairly under constrained  
under these conditions).

### 3 Results and discussion

#### 3.1 Emission factors

330 The elemental sulfur EFs calculated for FIREX-AQ are comparable to previous reports. As  
described in section 2.4, flaming and smoldering delineation was determined by an MCE value  
of 0.9. For consistency with other FIREX-AQ reports, the fuel types listed remain as  
subcategories, but are combined for comparison to the comprehensive biomass burning fuel  
335 types listed in Andreae (2019). The FIREX-AQ agriculture category comprises measurements of  
residual burns of rice, corn, and soybean fields. Across the fuel types measured during FIREX-  
AQ (Fig. 2), we find that  $\text{SO}_2$  is consistently larger than sulfate when calculated as EFs of  
elemental sulfur, indicating that, at most, a minor fraction of  $\text{SO}_2$  (20-25%) is converted to  
sulfate within 1 hr downwind (or emitted directly as primary sulfate). Where data is not reported,  
340 this is due to either missing data or a low correlation with total carbon ( $R^2 < 0.5$ ). The total sulfur  
EFs agree reasonably well with those reported by Andreae et al. (1988), measured in the Amazon  
basin, in the range of  $0.24$ - $0.66$  g S  $\text{kg}^{-1}$  C.



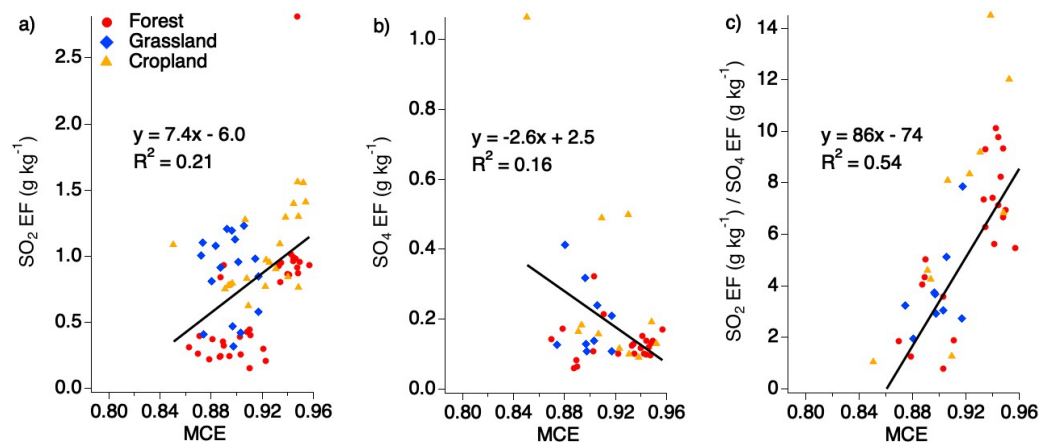
345 *Figure 2. Elemental sulfur emission factors of SO<sub>2</sub> and sulfate by fuel type and combustion stage within 1 hr downwind compared to literature values of total sulfur emission factors.*

No trend with MCE is observed for SO<sub>2</sub> EFs when separated by the various fuel types when considering fuel types with measurements of smoldering and flaming conditions as well as SO<sub>2</sub> and sulfate measurements above MCE 0.85 (Fig. 3). It has previously been suggested that  
350 EFs can be calculated based on MCE for use by the global climate modeling community. There have been conflicting opinions around this suggestion with some species showing relevant correlations while other species do not (Yokelson et al., 1996; Burling et al., 2011; Akagi et al., 2013). Considering all the EFs for SO<sub>2</sub>, sulfate, and the ratio of SO<sub>2</sub> to sulfate under one hour shows that, individually, SO<sub>2</sub> and sulfate do not show strong correlations with MCE (Fig. 3).  
355 However, the ratio of the two produces a stronger correlation suggesting there may be a relationship in which more sulfate may be produced during smoldering combustion and more SO<sub>2</sub> emitted during flaming combustion. One possibility is that the smoke plumes from smoldering fires are more conducive to rapid conversion of SO<sub>2</sub> to sulfate such that the ratio of SO<sub>2</sub> and sulfate has significantly decreased by the time it is sampled. This could be due to a  
360 number of factors, including higher aerosol EF which, depending on the aerosol composition, could allow for more rapid aqueous phase oxidation. It is also possible that more primary sulfate is emitted from those plumes.

Averaging the flaming and smoldering EFs produces an overall SO<sub>2</sub> EF of  $0.73 \pm 0.43$  g SO<sub>2</sub> kg<sup>-1</sup> C. This is within the combined variability of the Andreae (2019) compilation of flaming and smoldering EFs of  $0.62 \pm 0.75$  g kg<sup>-1</sup> C, which excludes peat and laboratory fires. Separating the SO<sub>2</sub> EFs by combustion stage results in a flaming stage value of  $0.80 \pm 0.46$  g kg<sup>-1</sup> C ( $0.62 \pm 0.61$  g kg<sup>-1</sup> C from Andreae, 2019) and a smoldering stage value of  $0.62 \pm 0.36$  g kg<sup>-1</sup> C ( $0.61 \pm 0.27$  g kg<sup>-1</sup> C from Andreae, 2019). While the FIREX-AQ flaming stage value is considerably higher than the Andreae (2019) compilation, the two are within the combined variability of the  
370 observations. However, this higher average EF for the flaming stage FIREX-AQ measurements



is strongly influenced by the large number of measurements of longleaf pine and agricultural fuels which had high EF values.



375 *Figure 3. Scatter plots of EFs for SO<sub>2</sub> (a), sulfate (b), and the ratio of SO<sub>2</sub> to sulfate (c) (within 1 hr downwind of each fire source) vs. MCE based on combined fuel types.*

Looking more closely at the different fuel types in comparison to the categories compiled by Andreae (2019), we see good agreement within the combined variability (Table 1 and Fig. 4).  
380 While the fuel types are categorized differently in this study, many still fit the characteristics of the categories listed in the compilation report allowing for comparison. Of the FIREX-AQ categories that allow for comparison with Andreae (2019), all EF data available are for the flaming stage.

The generally strong agreement between FIREX-AQ EFs and those in published  
385 inventories lends confidence to the quality of EFs underlying model emissions. Agricultural burns exhibit the highest EFs. This was reported by Andreae (2019) as  $0.80 \pm 0.71 \text{ g kg}^{-1} \text{ C}$  in the flaming stage, similar to  $1.1 \pm 0.30 \text{ g kg}^{-1} \text{ C}$  reported here. The temperate forest category, comprised here of forest and slash, produces a combined EF of  $0.70 \pm 0.51 \text{ g kg}^{-1} \text{ C}$  which is in excellent agreement with the Andreae (2019) value of  $0.7 \pm 0.48 \text{ g kg}^{-1} \text{ C}$ . Combining savanna, shrubland, grassland, and understory, into the savanna/grassland category produces the largest  
390 difference in which the FIREX-AQ value of these combined fuels is  $0.70 \pm 0.26 \text{ g kg}^{-1} \text{ C}$ , whereas, Andreae (2019) reported a value of  $0.47 \pm 0.44 \text{ g kg}^{-1} \text{ C}$ ; however, these values fit within the standard deviation.

395

400



405

*Table 1. Comparison of the flaming stage SO<sub>2</sub> EFs (g kg<sup>-1</sup> C) by fuel type as measured during FIREX-AQ (left) to the compiled values reported in Andreae (2019) (right).*

Fuel Type (FIREX-AQ)	EF	StDev	Num tran <sup>+</sup>	Combined Categories	EF	StDev	Num stud <sup>*</sup>	Fuel Type (Andreae, 2019)
Forest	0.66	0.49	35	0.70 ± 0.51	0.7	0.48	5	Temperate forest
Slash	1.15	0.38	3					
Savanna	0.47	0.06	2	0.70 ± 0.26	0.47	0.44	12	Savanna/grassland
Shrubland	0.56		1					
Grassland	0.83	0.29	6					
Understory	0.53		1					
Cropland	1.09	0.30	16	-	0.8	0.71	10	Agriculture

<sup>+</sup>Num tran indicates the number of transects measured within 1 hr downwind of the fire source measured during FIREX-AQ.

<sup>\*</sup>Num stud indicates the number of studies included in the Andreae (2019) compilation.

410 The categories measured during FIREX-AQ that do not overlap with the Andreae (2019)  
 compilation reflect smoldering conditions. For the most part, the majority of the smoldering  
 stage SO<sub>2</sub> EFs exhibit lower values than the flaming stage by approximately 21-63% (Fig. 4).  
 The two FIREX-AQ categories (grassland and understory) which show smoldering SO<sub>2</sub> EFs to  
 be larger than the flaming stage suggest the need for additional measurements to build statistical  
 415 confidence.

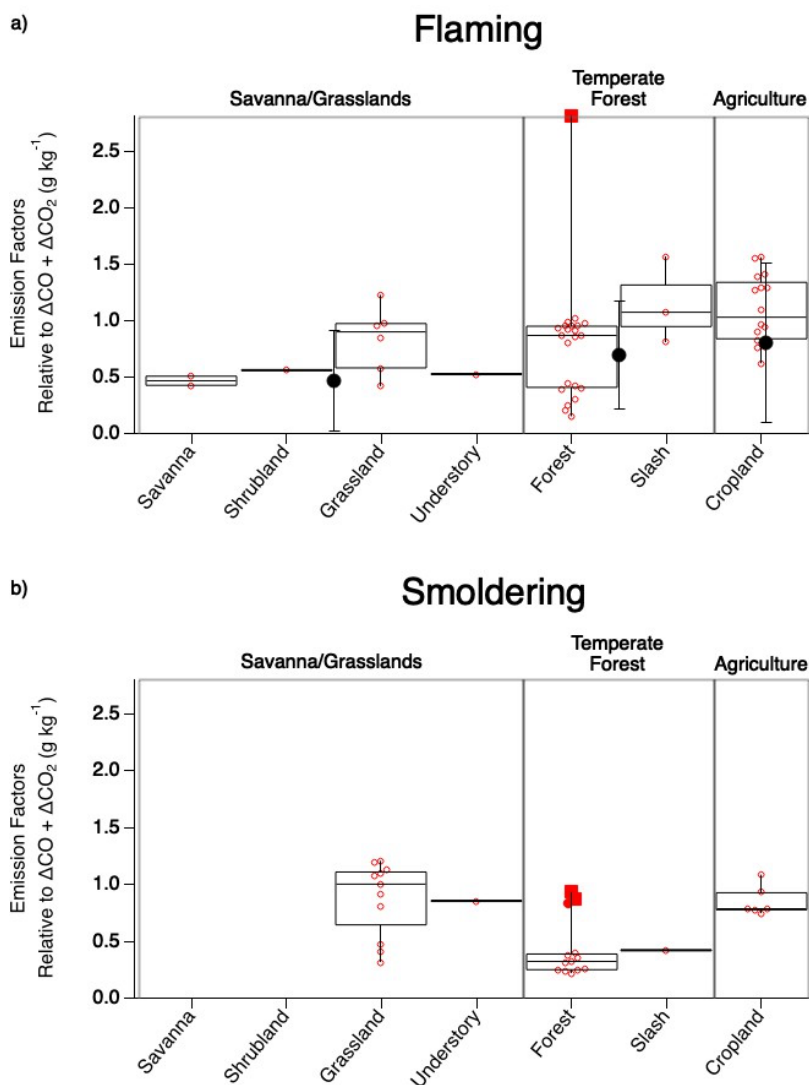


Figure 4. Comparison of  $\text{SO}_2$  EF values observed during flaming (a) and smoldering (b) combustion across fuel types sampled during FIREX-AQ. The box upper edge represents the 75<sup>th</sup> percentile and the lower edge the 25<sup>th</sup> percentile with the median shown by the middle line. The whiskers represent the minimum and maximum observed values with the open circles representing each observation and the solid red circle representing a potential outlier. The large solid black circles with error bars depicting 1 standard deviation in panel (a) show corresponding average Andreae (2019) values.

420  
425



### 3.2 Emission factor variability

430

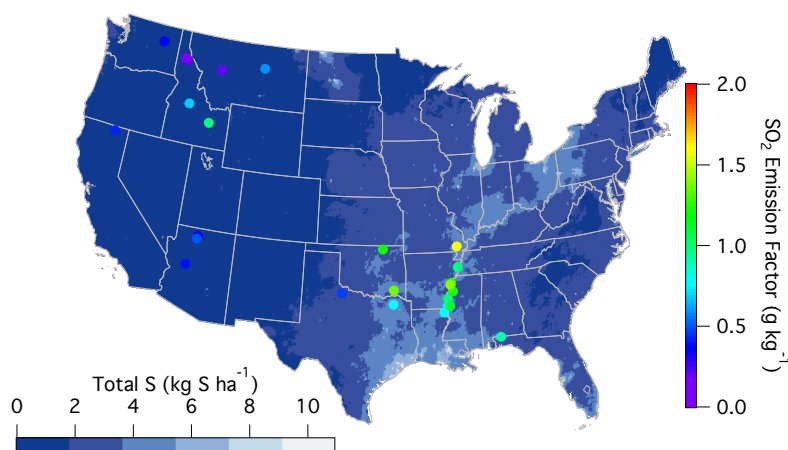
The variability observed amongst the different fuel types may partly reflect variability in surface S content stemming from wet and dry deposition. Although this source of sulfur has significantly decreased in the U.S. over the last two decades, the highest emission factors during FIREX-AQ were observed within the regions of the U.S. that typically experience the largest sulfur deposition rates as reported by the National Atmospheric Deposition Program (2022) (Fig. 5).

435

Sulfur-containing fertilizers may also enhance S content in smoke. Sulfur aids plant uptake of nitrogen, and decreasing sulfur deposition over the last two decades has led to an increased use of sulfur additives in fertilizers (Hinckley et al., 2020). Hinckley et al. (2020) report this sulfur application to range from around 20-300 kg S ha<sup>-1</sup> yr<sup>-1</sup>, which occurs in the form of inorganic sulfate or elemental sulfur (Solberg et al., 2011). Given that the average yield of corn within the U.S. is 168 bushels per acre, a sulfur application of 20 kg S ha<sup>-1</sup> yr<sup>-1</sup> would result in 12 g S kg<sup>-1</sup> C in its composition. Assuming 10% of this added sulfur remains after harvest and runoff and is present in the residual material that is burned, the remaining 1.2 g S kg<sup>-1</sup> could in part explain the enhanced emission factors in those regions (U.S. Department of Agriculture, 2020). Therefore, the observed variability in emission factors throughout the U.S. may be in part explained by the sulfur availability to the plants and soils, either from deposition or fertilizer use, resulting in larger emission factors from certain locations when burned.

440

445



450

Figure 5. National Atmospheric Deposition Program (2022) reported sulfur deposition rates (<https://nadp.slh.wisc.edu/committees/tdep/#tdep-maps>) compared to SO<sub>2</sub> EFs (closed circles) by geographical location as measured during FIREX-AQ for all fuel types.

### 4 Chemical Evolution of Sulfur

455

After emission, SO<sub>2</sub> oxidizes to sulfate via both gas and condensed-phase processes. Discrepancies reported by previous studies of modeled sulfate compared to measurements suggest that the conversion chemistry of SO<sub>2</sub> to sulfate is not fully understood. In this section, we combine FIREX-AQ observations with a detailed chemical box model to evaluate the chemical mechanisms of SO<sub>2</sub> to sulfate conversion.

460



#### 4.1 Temperature dependence of sulfate production efficiency

The balance of gas and particle phase sulfur between SO<sub>2</sub> and sulfate exhibits a marked temperature dependence amongst the cumulative flights while remaining generally constant during individual flights (Fig. 6). Sulfate is >90% of the sum at temperatures below 265K, while above 285 K SO<sub>2</sub> and sulfate are equally balanced which is likely due to the quasi-second order process of heterogeneous oxidation in a plume (Freiberg, 1978). The noisy, but overall positive trend between 265-283 K suggests rapid chemistry after emission. Conversion of SO<sub>2</sub> to sulfate generally increases with decreasing temperature due to increased aerosol water content and SO<sub>2</sub> and oxidant solubility, but the rapid change observed in this temperature regime also requires aqueous phase sulfur oxidation (Pattantyus et al., 2018).

The majority of sulfur oxidation occurs in the aqueous phase. As observed during the 3 August flight, calculation of the contribution of OH to the decrease in SO<sub>2</sub> by applying an OH concentration of  $2 \times 10^6 \text{ cm}^{-3}$  (Liao et al., 2021) produces a negligible SO<sub>2</sub> decay compared to the dilution normalized mixing ratio of SO<sub>2</sub> (Fig. S2). Similar behavior is expected for other flights due to similar conditions of limited photolysis near the center of the smoke plume.

Recent studies have suggested HCHO to be an important aqueous phase oxidant at reduced temperatures (Moch et al., 2018; Song et al., 2021). However, HCHO is also an indicator of smoke age with mixing ratios typically being largest nearest to the fire source (Liao et al., 2021). Considering measurements acquired when the HCHO mixing ratio is high (>25 ppb), implicitly filtering out aged smoke, the slope of the SO<sub>2</sub> to total sulfate ratio over the 265-283 K temperature regime (0.04) shows a stronger correlation with temperature ( $R^2=0.74$ ) (Fig. 6b, black line). Further limiting the effect of chemical aging by analyzing only those measurements within 1 hr of the fire source, the conversion of SO<sub>2</sub> to sulfate is observed to be approximately 65% slower (Fig. 6b, red line) in the 265-283 K temperature range. This is consistent with heterogeneous chemistry in that aging occurs more rapidly at higher temperatures. While sulfate measurements within 1 hr of the fire source could be due to primary emission, this is expected to be a small fraction compared to SO<sub>2</sub> as shown in Fig. 2 and primary emission would not exhibit the temperature dependence observed here.

Other sulfate species are contributing to sulfur conversion during this temperature regime. There were several periods identified during these flights in which organosulfur species were recognized to be a significant fraction of the AMS sulfate measurement. These measurements only occurred within the temperature range 270-285 K. When organosulfur was present in plume transects within 1 hr downwind of the fire source, the SO<sub>2</sub> to total S ratio decreased with decreasing temperature 23% faster than in transects of fresh plumes when organosulfur was not present.

These findings emphasize the importance of temperature in combination with smoke age and organosulfur production on the conversion of SO<sub>2</sub> to sulfate and is further investigated in section 4.2.1.

500

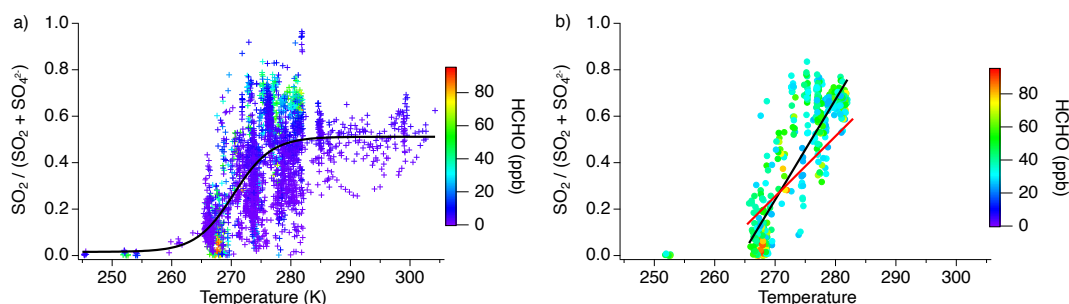


Figure 6. Fractional sulfur conversion as a function of temperature a) including all smoke ages with a sigmoid fit and b) only measurements with HCHO > 25 ppb with the black line indicating the linear fit through the data at all ages between 265–283 K and the red line indicating the linear fit through the measurements within 1 hr of emission in the same temperature regime.

505

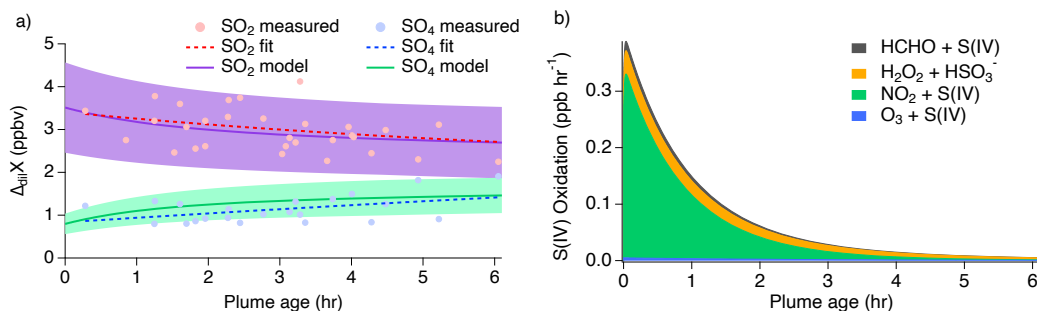
## 4.2 Model results

### 4.2.1 Williams Flats 3 August 2019 flight

510

Select time series relating to the conversion of SO<sub>2</sub> to sulfate for the 3 August 2019 flight are shown in Fig. S3. Altitude and temperature were constant, around 3 km and 280 K, for both passes of about 10 transects each. Actinic fluxes trended downward for the second pass as dusk approached. Thermodynamic modeling suggests an average pH value of 5.3 (range of -2 to 8) over the length of the plume transects, but a possible increase in LWC by a factor of 2–3 during the second pass. Because the conditions of this flight are relatively consistent between passes, the measurements of both passes are combined for comparison to the model with pH and LWC held constant. Modeling results of this flight with the inclusion of all known gas- and aqueous-phase S(IV) oxidation pathways (Table S1) are shown in Fig. 7 with a conservatively assumed 30% uncertainty shown. This uncertainty range encompasses the uncertainties associated with the mechanism of aqueous phase uptake and chemical rate constants occurring at the specified LWC and pH.

520



525

Figure 7. (a) Measurements of 3 August 2019 shown by the markers and measurement fits shown by the dashed lines compared to the SO<sub>2</sub> and sulfate model results represented by the solid lines with shading denoting an estimated 30% model uncertainty. The sulfate (SO<sub>4</sub>) measurements



530 *represent total sulfate which potentially includes organosulfur. (b) Stacked modeled S(IV)  
oxidation rates leading to sulfate and HMS production.*

The model reproduces the general measurement trend of the 3 August flight for both SO<sub>2</sub> and sulfate (Fig. 7a). Model results for NO, NO<sub>2</sub>, NO/NO<sub>2</sub>, O<sub>3</sub>, HCHO, and H<sub>2</sub>O<sub>2</sub> are compared to the measurements for each model in Fig. S4 showing good agreement for the 3 August flight.  
535 In accordance with the sulfate measurements, the modeled sulfate represents the sum of sulfate and HMS (the latter representing OS). Under the conditions of this flight, the model indicates that aqueous phase oxidation by NO<sub>2</sub> and H<sub>2</sub>O<sub>2</sub> are the dominant pathways leading to inorganic sulfate formation with little S(IV) oxidation by HCHO and O<sub>3</sub> (Fig. 7b). This is in contrast to what has been previously expected of aerosol S(IV) oxidation which has been thought to be  
540 dominated by ozone oxidation. However, the higher NO<sub>2</sub> oxidation rate constant with increased pH reported by Liu and Abbatt (2021) for non-ideal solutions increases the significance of this reaction.

#### 4.2.2 Williams Flats 7 August 2019 flight

545 The 7 August 2019 flight shows distinct differences between the two passes (Fig. S5); therefore, the flight has been differentiated into the first pass (first full set of transects) and second pass (second full set of transects). It is also during this flight that the largest OS contribution has been reported for the AMS measurements during the FIREX-AQ wildfire flights.

550 The first pass was measured around 4 km and 276 K with an estimated dilution factor of approximately  $8 \times 10^{-5} \text{ s}^{-1}$  and limited cloud presence. A pH of around 7.2 was estimated for this flight with an aerosol LWC of approximately  $1 \times 10^{-7} \text{ g m}^{-3}$ . Both NO<sub>2</sub> and CO decrease at similar rates while HCHO remains relatively stable around 40 ppb and O<sub>3</sub> shows a decrease compared to the air outside of the plume for the first six transects (Fig. S6). SO<sub>2</sub> and sulfate are  
555 fairly similar with a few instances of sulfate surpassing SO<sub>2</sub> in addition to a moderate fraction of OS observed during this pass.

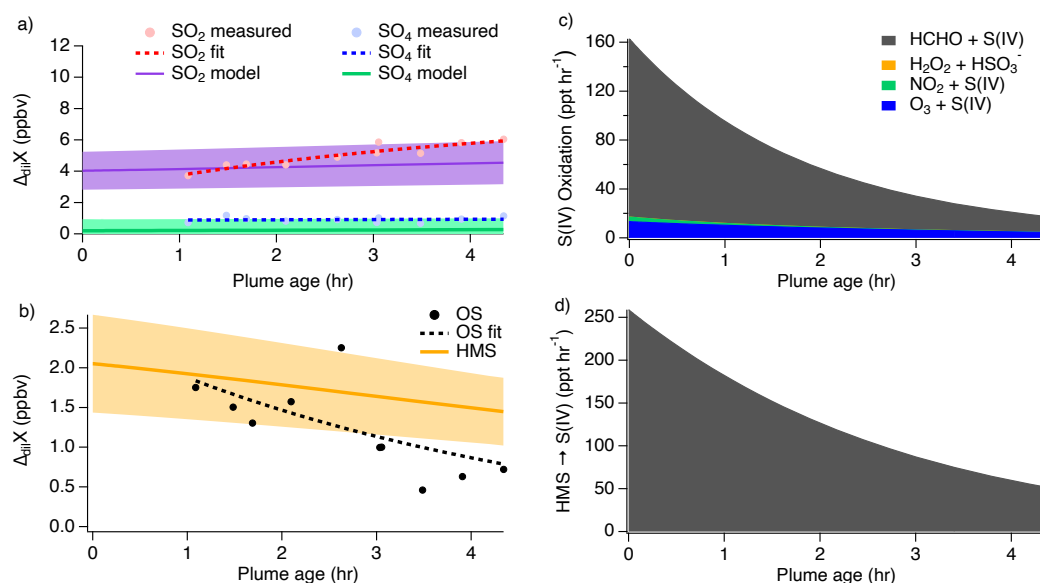
The rise in altitude for the second pass is associated with an 8 K decrease in temperature relative to the first pass. The dilution factor for this pass was determined to be slower at around  $3 \times 10^{-5} \text{ s}^{-1}$ . The difference in these dilution factors could be due to measuring at different  
560 altitudes or the result of a sampling artifact due to measuring in different sections of the plume, however, there is not enough information available to determine the exact cause. NO<sub>2</sub> appears to decrease more slowly in comparison to CO which remains relatively constant after the plume has moved away from the clouds. In addition, ozone, which shows the same trend as O<sub>x</sub>, appears to be consumed more quickly in transects in which clouds were observed, suggesting rapid uptake within the clouds, in addition to the fast reaction with NO producing the additional NO<sub>2</sub>. This  
565 additional NO<sub>2</sub> in combination with limited photochemistry as a result of decreasing actinic flux (Fig. S7) due to approaching dusk conditions slows the decreasing NO<sub>2</sub> trend observed during this pass. Furthermore, ISORROPIA calculations indicate a 10-fold increase in aerosol LWC in the presence of clouds compared to the first pass. This is likely due to the decrease in  
570 temperature (268 K) and larger relative humidity. The presence of clouds decreases downwind concurrently with a decrease in relative humidity, but aerosol LWC remains high. Lastly, this pass shows SO<sub>2</sub> is nearly depleted in the center of the plume (Fig. S5) while sulfate increases substantially with a rather significant fraction of OS being observed (Fig. S8).



575 Due to these distinct differences between passes, each pass was modeled separately with  
the OS contribution reported independently from the sulfate measurements and model results.  
The modeled oxidation compounds (Fig. S4) show generally good agreement with the  
measurements for these passes; however, some discrepancies are observed due to measuring  
different parts of the plume. Results of the first pass are shown in Fig. 8 and the second pass  
shown in Fig. 9, both showing good agreement between the model and measurements with ozone  
580 and NO<sub>2</sub> as the largest contributors to sulfate production during this flight. However, the  
majority of modeled S(IV) oxidation occurs through the HCHO pathway rapidly producing  
HMS.

The first pass shows SO<sub>2</sub> increasing downwind, which is unexpected because SO<sub>2</sub> is  
585 considered to be a primary emission which typically decreases downwind as it is removed  
through oxidation. In addition, the measurements show a large OS mixing ratio following the  
first hour after emission before gradually decreasing downwind. This suggests that OS is either  
directly emitted from the fire source or very rapidly produced.

Clouds and large LWC were present throughout the majority of the second pass  
measurements (Figs. S5 and S6), significantly shifting the chemistry from that of the first pass.  
590 Figure 9 shows that modeled SO<sub>2</sub> is quickly taken up into the aqueous phase under these higher  
LWC conditions with approximately 1.5 ppbv going directly into sulfate production and the  
remaining 3 ppbv of the initial SO<sub>2</sub> concentration being converted into HMS. These oxidation  
processes occur promptly after emission, but they rapidly slow once all of the available initial  
SO<sub>2</sub> is depleted within the first 1-2 minutes. The exponential trends of the sulfate and OS  
595 measurements agree with the model results to within approximately 40%.

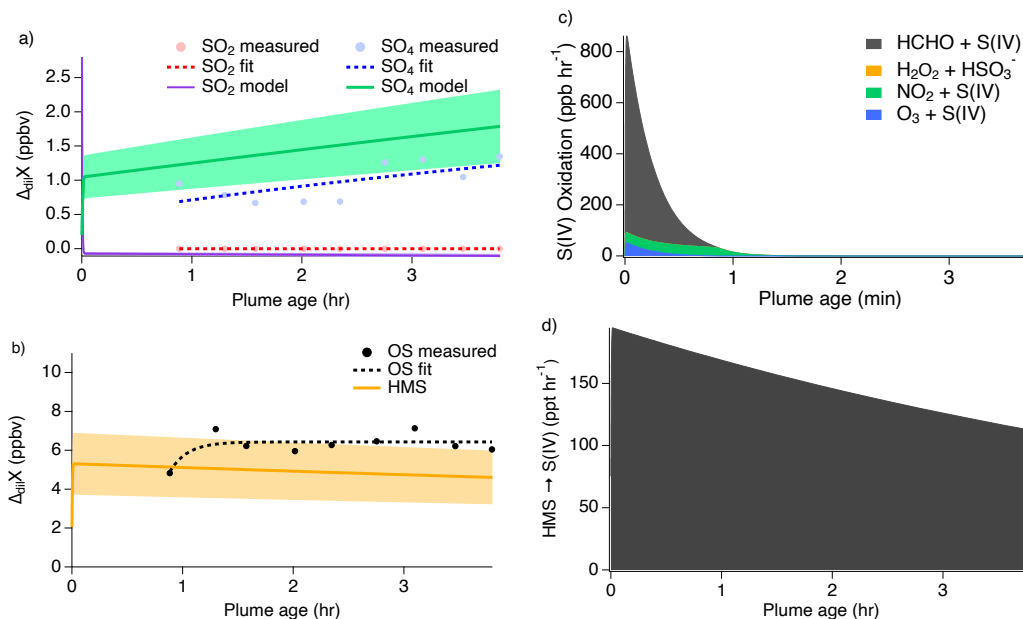


600 Figure 8. First pass measurements shown by the markers and measurement fits shown by the dashed lines compared to the model results represented by the solid lines with shading denoting an estimated 30% model uncertainty for SO<sub>2</sub> and sulfate (a) and OS (b). Stacked modeled S(IV)



605

oxidation rates (c) leading to sulfate and HMS production. HMS reverse reaction rate (d) reproducing S(IV).



610

Figure 9. Second pass measurements shown by the markers and measurement fits shown by the dashed lines compared to the model results represented by the solid lines with shading denoting an estimated 30% model uncertainty for SO<sub>2</sub> and sulfate (a) and OS (b). Stacked modeled S(IV) oxidation rates (c) leading to sulfate and HMS production. HMS reverse reaction rate (d) reproducing S(IV).

615

The importance of HMS as a S(IV) reservoir and its conversion into sulfate or into gas-phase SO<sub>2</sub> largely depends on the varying conditions of LWC. Under neutralized conditions (7.2), the model reproduces the observed trends of all three compounds for the first pass at low aerosol LWC ( $1 \times 10^{-7} \text{ g m}^{-3}$ ) and for the second pass at LWC conditions typical of wet aerosol ( $1 \times 10^{-3} \text{ g m}^{-3}$ ). As discussed further in section 4.2.3, the higher pH of this flight increases the rate of HMS reversal back into S(IV) by a factor of six. Because of the low LWC of the first pass, heterogeneous uptake is limited and causes the rates of S(IV) oxidation to significantly decrease. S(IV) evaporation then enhances gas phase SO<sub>2</sub> in transported smoke, consistent with similar rates of HMS decay and SO<sub>2</sub> growth. As a result, very little sulfate is produced during this pass at a rate of approximately 4 ppt hr<sup>-1</sup> primarily due to S(IV) oxidation by ozone.

620

625

However, the higher LWC conditions of the second pass allow S to remain in the aqueous phase. The small increase in sulfate of approximately 500 ppt over the course of the flight can be explained by a small fraction of HMS, on the order of 120-190 ppt hr<sup>-1</sup>, which undergoes a reverse reaction decomposing back into S(IV) before being oxidized to produce sulfate (Fig. 9d).

630

The SAGA instrument detects HMS as S(IV), which cannot be separated from HSO<sub>3</sub><sup>-</sup> and SO<sub>3</sub><sup>+</sup> and is therefore subject to interference from high concentrations of gas-phase SO<sub>2</sub>. As shown in Fig. S8, MC sulfate measurements show similar concentrations to the AMS organosulfur portion of the total sulfate measurements during the first pass, but a considerably



635 smaller value in comparison during the second pass. This suggests that HMS may have been the majority of the organosulfur concentrations measured during the first pass but that an additional unknown organosulfur was much more abundant than HMS during the second pass. Therefore, it appears that the modeled HMS exceeds measurements on the second pass.

640 There are two potential explanations for the good agreement between the observed organosulfur concentration from the second pass and the modeled HMS. It is possible that during the very rapid uptake of SO<sub>2</sub> into the aqueous phase, (1) additional organosulfur species may be produced or (2) the additional organosulfur species are the result of further reactions of HMS suggesting that the model is correctly reproducing the HMS formation chemistry, but indicating that the model aqueous phase chemistry is incomplete. Both of these potential explanations require that the measured organosulfur species behave similarly to HMS in their rates of formation and termination in order to explain the good agreement between the modeled HMS and measured organosulfur concentrations. In addition, these explanations would require that the  
645 organosulfur species are not identified as S(IV) in ion chromatography measurements. While the modeling allows for significant insight into the identity and formation mechanisms of aerosol sulfur, there is not enough evidence available from these measurements to conclusively explain all of the AMS and SAGA sulfur observations.

#### 650 4.2.3 Model HMS sensitivity analysis

We performed a model sensitivity analysis to investigate the relevance of organosulfur behavior under the conditions of the HMS rates of production and termination in different environments by varying the model LWC (10<sup>-6</sup> - 1 g m<sup>-3</sup>), pH (1-8), temperature (260-280 K), and HCHO (10-90 ppb) individually while holding the other parameters constant at the 3 August flight  
655 conditions (T = 280 K, pH = 5.3, and LWC = 2 × 10<sup>-4</sup> g m<sup>-3</sup>) due to the more simplified chemistry occurring during this flight.

Variations in LWC (Fig. 10a) show that aerosols with less LWC produce minimal amounts of sulfate and HMS, but that HMS makes up between 5 and 45% of the combined  
660 concentrations. The HMS fraction shows the largest contribution as LWC increases into the cloud regime at which point sulfate production begins to decrease with a rapid increase in HMS. While the typical LWC range estimated for these fires is 10<sup>-7</sup> – 10<sup>-2</sup> g m<sup>-3</sup>, this indicates that the chemistry of the smoke will change substantially with cloud interactions. LWC is shown to be an important variable in the ratio of the formation of HMS to sulfate; however, this ratio trend is indicative of conditions at pH 5.3 and will vary under differing pH conditions.  
665

The pH dependence of the ratio of HMS / (SO<sub>4</sub> + HMS) is shown in Fig. 10b in which HMS formation is more active as the acidity decreases. At acidic pH values, representative of typical tropospheric aerosol (Nault et al., 2021), a negligible amount of HMS contributes to the combined concentrations. Above pH 4, HMS contribution begins to increase followed by a more  
670 rapid increase after pH 6. The maximum HMS contribution is reached around pH 7.3 before rapidly decreasing at higher values.

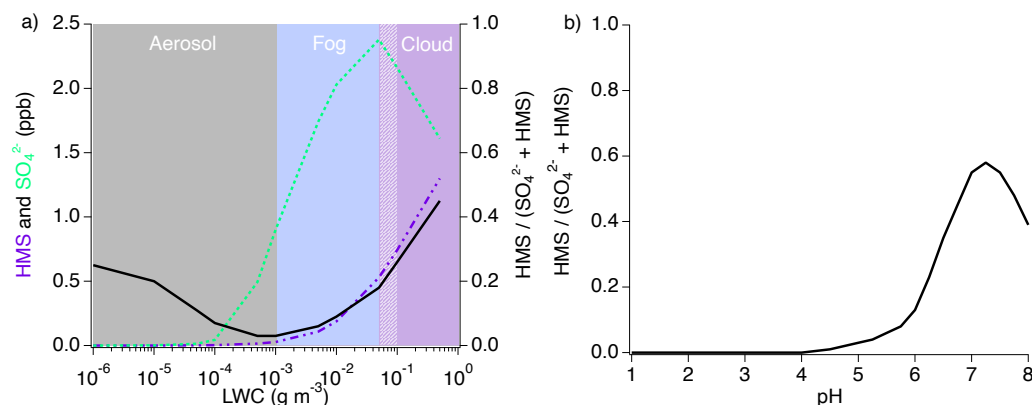
The ratio of HMS production and reverse reactions varies with pH with the reverse reaction becoming more substantial at higher pH (Fig. 11). Under aerosol LWC conditions, the rate of the HMS reverse reaction is up to 3 times larger than the rate of HMS production. As  
675 LWC increases into the cloud regime, the rate of the HMS reverse reaction increases further to approximately two orders of magnitude larger than HMS production around pH 7. However, a



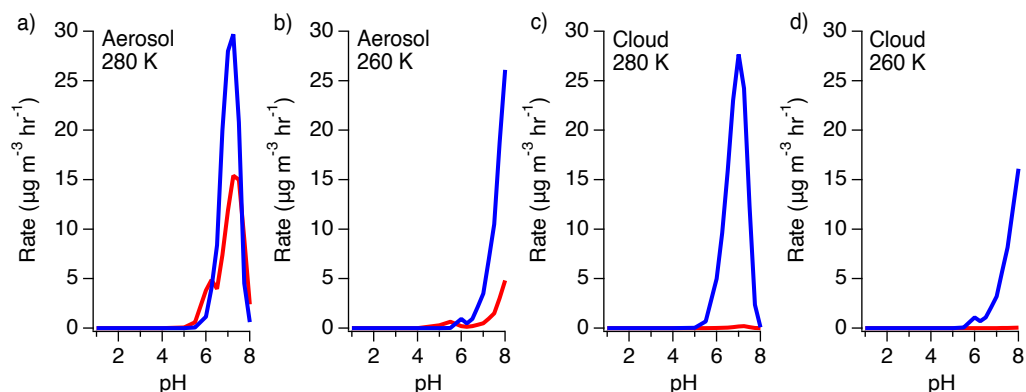
reduction in temperature shifts this dependence to higher pH decreasing the rate of HMS reversal at the same pH.

680 While temperature and HCHO concentration are key factors controlling HMS production, these factors alone under low LWC and pH result in minimal HMS (Fig. S9). HMS production increases with decreasing temperature; however, under the conditions of the 3 August flight, HMS only reaches a maximum value of 5 ppt at 260 K which is approximately 5% of the modeled sulfate. Similarly, a minimal amount of HMS is produced with varied HCHO, but the ratio of HMS to the sum of HMS and sulfate increases linearly with HCHO at a rate of 1.5 ppt  
685  $\text{ppb}^{-1}$  HCHO.

The conditions that most largely affect HMS are LWC and pH. Due to the significance of LWC to HMS production and reversal, it is likely that aqueous aerosols, fog, cloud droplets, and possibly ice crystals will be most impactful on HMS production. Because the rainwater pH of areas such as the Western U.S. and Eastern China can reach much less acidic pH levels due to increased ammonia emissions, it is likely that these areas will be more susceptible to HMS  
690 production (Keresztesi et al., 2020; Qu and Han, 2021). Together, these conditions indicate that highly polluted areas which experience higher pH and greater LWC will likely be influenced by this chemistry. Therefore, the production of HMS should be an important consideration for air quality in areas such as agricultural regions which experience enhanced emissions of ammonia,  
695 likely increasing the pH, as well as geographical locations which may promote fog formation. This would include areas such as Beijing, the Uintah basin, and Bakersfield, CA which have observed severe haze formation and have the potential to be affected by HMS.



700 Figure 10. Sensitivity analysis of HMS formation under individually varied LWC and pH conditions. The black line in each figure represents the ratio of the modeled HMS mixing ratio to the sum of the modeled inorganic sulfate and HMS. The shading in b) reflects the typical rainwater pH for each region.



705

Figure 11. Rates of HMS production (red) and reversal (blue) under aerosol and cloud conditions at 280 K and 260 K.

## 710 5. Conclusions

SO<sub>2</sub> plays an important role in sulfate aerosol formation and thus air quality and climate forcing. Therefore, understanding the sources and evolution of SO<sub>2</sub> emissions in a changing climate are essential. The emission factors determined from the FIREX-AQ mission under flaming conditions show good agreement with the compilation reported by Andreae (2019). This provides confidence for the same categories under smoldering conditions for which there are no reported measurements from previous studies. No distinct correlation is observed for SO<sub>2</sub> emission factors based on MCE; however, it remains unclear if fire MCE influences the ratio of SO<sub>2</sub> and sulfate emission factors. With biomass burning events increasing worldwide, this study suggests that the resulting SO<sub>2</sub> emission factors will be more dependent on geographical location and land use, and less dependent on combustion phase and fuel type. Areas that incur more sulfur deposition from coal burning or application through fertilizer use, will likely produce larger SO<sub>2</sub> emission factors.

Modeling with inclusion of the HCHO oxidation chemistry, producing HMS, shows good agreement with the measurements. However, the differentiation of HMS from sulfate through the SAGA measurements indicates that HMS can be over-predicted. While HMS is potentially directly emitted from the fire source, a large organosulfur concentration is observed that has not yet been identified. Because the modeled HMS is similar to the measured organosulfur fraction, it is expected that the additional organosulfur species likely exhibit similar rates of production and termination as HMS. The importance of the HMS, or similar species, reverse reaction is also made apparent by the ability to act as an S(IV) reservoir. This allows these species to produce sulfate or SO<sub>2</sub> further downwind depending on the LWC and pH.

Environments that experience high LWC and pH are expected to be the most influenced by this chemistry. This includes regions that experience higher ammonia emissions and are geographically or meteorologically subject to greater cloud or fog formation. As a result, this chemistry should be considered when assessing severe haze events as a result of either biomass burning or industrial pollution.

## Plain Language Summary



740

Biomass burning sulfur dioxide (SO<sub>2</sub>) emission factors range from 0.27–1.1 g kg<sup>-1</sup> C. Biomass burning SO<sub>2</sub> can quickly form sulfate and organosulfur, but these pathways are dependent on liquid water content and pH. Hydroxymethanesulfonate (HMS) appears to be directly emitted from some fire sources, but is not the sole contributor to the organosulfur signal. It is shown that HMS and organosulfur chemistry may be an important S(IV) reservoir with the fate dependent on the surrounding conditions.

745

### Keywords

750 Sulfur dioxide, hydroxymethanesulfonate, emission factors, biomass burning

*Data and code availability.* The data collected for FIREX-AQ are available from the NASA/NOAA FIREX-AQ data archive: <https://www-air.larc.nasa.gov/cgi-bin/ArcView/firexaq>. The Framework for 0-D Atmospheric Modeling code is available from the AirChem/F0AM archive: <https://github.com/AirChem/F0AM> (doi.org/10.5281/zenodo.5752566).

755

*Author contribution.* The research was designed by PSR and AWR. Measurement contributions were provided by all authors. The modeling was performed by PSR and GMW. The paper was written by PSR with contributions from all coauthors.

760

*Competing interests.* The authors declare that they have no conflict of interest.

*Acknowledgements.* P.S.R. and A.W.R. acknowledge support from NASA's Upper Atmosphere Composition Observations program. MD, MS, and BW have received funding from the European Research Council (ERC) under the European Union's Horizon 2020 research and innovation framework programme under grant agreement No. 640458 (A-LIFE), and from University of Vienna. HG, PCJ, and JLJ were supported by NASA 80NSSC18K0630 and 80NSSC21K1451 and NSF AGS-1822664. GMW, TFH, RAH, JMS, and JL acknowledge support from the NASA Tropospheric Composition program and the NOAA AC4 program (NA17OAR4310004). SRH and KU are funded under NASA grant 80NSSC18K0638. The National Center for Atmospheric Research is sponsored by the National Science Foundation. We would like to thank the NASA DC-8 crew and management team for support during FIREX-AQ integration and flights. Data from FIREX-AQ are available at (<https://www-air.larc.nasa.gov/cgi-bin/ArcView/firexaq>).

775

### References

Adachi, K., Dibb, J. E., Scheuer, E., Katich, J. M., Schwarz, J. P., Perring, A. E., Mediavilla, B., Guo, H., Campuzano-Jost, P., Jimenez, J. L., Crawford, J., Soja, A. J., Oshima, N., Kajino, M., Kinase, T., Kleinman, L., Sedlacek III, A. J., Yokelson, R. J., Buseck, P. R.: Fine Ash-Bearing Particles as a Major Aerosol Component in Biomass Burning Smoke, *J. Geophys. Res. Atmos.*, 127(2), <https://doi.org/10.1029/2021JD035657>, 2022.

780

Akagi, S. K., Yokelson, R. J., Burling, I. R., Meinardi, S., Simpson, I., Blake, D. R., McMeeking, G. R., Sullivan, A., Lee, T., Kreidenweis, S., Urbanski, S., Reardon, J., Griffith, D.

785



- W. T., Johnson, T. J., and Weise, D. R.: Measurements of reactive trace gases and variable O<sub>3</sub> formation rates in some South Carolina biomass burning plumes, *Atmos. Chem. Phys.*, 13, 1141–1165, <https://doi.org/10.5194/acp-13-1141-2013>, 2013.
- 790 Albrecht, B. A.: Aerosols, cloud microphysics, and fractional cloudiness, *Science*, 245, 1227–1230, 1989.
- Andreae, M. O., Browell, E. V., Garstang, M., Gregory, G. L., Harriss, R. C., Hill, G. F., Jacob, D. J., Pereira, M. C., Sachse, G. W., Setzer, A. W., Silva Dias, P. L., Talbot, R. W., Torres, A. L., Wofsy, S. C.: Biomass-Burning Emissions and Associated Haze Layers Over Amazonia, *J. Geophys. Res. Atmos.*, 93(D2), 1509–1527, <https://doi.org/10.1029/JD093iD02p01509>, 1988.
- 795
- Andreae, M. O.: Emission of trace gases and aerosols from biomass burning – an updated assessment, *Atmos. Chem. Phys.*, 19, 8523–8546, <https://doi.org/10.5194/acp-19-8523-2019>, 2019.
- 800
- Brock, C. A., Wagner, N. L., Anderson, B. E., Attwood, A. R., Beyersdorf, A., Campuzano-Jost, P., Carlton, A. G., Day, D. A., Diskin, G. S., Gordon, T. D., Jimenez, J. L., Lack, D. A., Liao, J., Markovic, M. Z., Middlebrook, A. M., Ng, N. L., Perring, A. E., Richardson, M. S., Schwarz, J. P., Washenfelder, R. A., Welti, A., Xu, L., Ziemba, L. D., and Murphy, D. M.: Aerosol optical properties in the southeastern United States in summer &ndash; Part 1: Hygroscopic growth, *Atmos. Chem. Phys.*, 16, 4987–5007, 2016.
- 805
- Burling, I. R., Yokelson, R. J., Griffith, D. W. T., Johnson, T. J., Veres, P., Roberts, J. M., Warneke, C., Urbanski, S. P., Reardon, J., Weise, D. R., Hao, W. M., and de Gouw, J.: Laboratory measurements of trace gas emissions from biomass burning of fuel types from the southeastern and southwestern United States, *Atmos. Chem. Phys.*, 10, 11115–11130, <https://doi.org/10.5194/acp-10-11115-2010>, 2010.
- 810
- Burling, I. R., Yokelson, R. J., Akagi, S. K., Urbanski, S. P., Wold, C. E., Griffith, D. W. T., Johnson, T. J., Reardon, J., and Weise, D. R.: Airborne and ground-based measurements of the trace gases and particles emitted by prescribed fires in the United States, *Atmos. Chem. Phys.*, 11, 12197–12216, <https://doi.org/10.5194/acp-11-12197-2011>, 2011.
- 815
- Canagaratna, M. R., Jayne, J. T., Jimenez, J. L., Allan, J. D., Alfarra, M. R., Zhang, Q., Onasch, T. B., Drewnick, F., Coe, H., Middlebrook, A., Delia, A., Williams, L. R., Trimborn, A. M., Northway, M. J., Decarlo, P. F., Kolb, C. E., Davidovits, P., and Worsnop, D. R.: Chemical and microphysical characterization of ambient aerosols with the Aerodyne Aerosol Mass Spectrometer, *Mass Spectrom. Rev.*, 26, 185–222, 2007.
- 820
- 825 Chan, C.K., Yao, X.: Air pollution in mega cities in China. *Atmospheric Environment* 42, 1–42, 2008.
- Cheng, Y., Zheng, G., Wei, C., Mu, Q., Zheng, B., Wang, Z., Gao, M., Zhang, Q., He, K., Carmichael, G., Pöschl, U., and Su, H.: Reactive nitrogen chemistry in aerosol water as a source
- 830



- of sulfate during haze events in China, *Sci. Adv.*, 2(12) 1-11, DOI: 10.1126/sciadv.1601530, 2016.
- 835 D'Ambro, E. L., Moller, K. H., Lopez-Hilfiker, F. D., Schobesberger, S., Liu, J., Shilling, J. E., Lee, B. H., Kjaergaard, H. G., and Thornton, J. A.: Isomerization of Second-Generation Isoprene Peroxy Radicals: Epoxide Formation and Implications for Secondary Organic Aerosol Yields, *Environ. Sci. Technol.*, 51(9), 4978-4987, <https://doi.org/10.1021/acs.est.7b00460>, 2016.
- 840 Day, D. A., Campuzano-Jost, P., Nault, B. A., Palm, B. B., Hu, W., Guo, H., Wooldridge, P. J., Cohen, R. C., Docherty, K. S., Huffman, J. A., de Sá, S. S., Martin, S. T., and Jimenez, J. L.: A Systematic Re-evaluation of Methods for Quantification of Bulk Particle-phase Organic Nitrates Using Real-time Aerosol Mass Spectrometry, *Atmos. Meas. Tech.*, <https://doi.org/10.5194/amt-15-459-2022>, 2022.
- 845 DeCarlo, P. F., Kimmel, J. R., Trimborn, A., Northway, M. J., Jayne, J. T., Aiken, A. C., Gonin, M., Fuhrer, K., Horvath, T., Docherty, K. S., Worsnop, D. R., and Jimenez, J. L.: Field-deployable, high-resolution, time-of-flight aerosol mass spectrometer, *Anal. Chem.*, 78, 8281–8289, <https://doi.org/10.1021/ac061249n>, 2006.
- 850 Dibb, J. E., Talbot, R. W., Seid, G., Jordan, C., Scheuer, E., Atlas, Elliot, Blake, N. J., and Blake, D. R.: Airborne sampling of aerosol particles: Comparison between surface sampling at Christmas Island and P-3 sampling during PEM-Tropics B, *J. Geophys. Res.-Atmos.*, 108, 8230–8230, doi:10.1029/2001JD000408, 2002.
- 855 Dovrou, E., Lim, C. Y., Canagaratna, M. R., Kroll, J. H., Worsnop, D. R., and Keutsch, F. N.: Measurement techniques for identifying and quantifying hydroxymethanesulfonate (HMS) in an aqueous matrix and particulate matter using aerosol mass spectrometry and ion chromatography, *Atmos. Meas. Tech.*, 12, 5303–5315, <https://doi.org/10.5194/amt-12-5303-2019>, 2019.
- 860 Farmer, D. K., Matsunaga, A., Docherty, K. S., Surratt, J. D., Seinfeld, J. H., Ziemann, P. J., and Jimenez, J. L.: Response of an aerosol mass spectrometer to organonitrates and organosulfates and implications for atmospheric chemistry, *Proc. Natl. Acad. Sci. U. S. A.*, 107, 6670–6675, 2010.
- 865 Feinberg, A., Sukhodolov, T., Luo, B. P., Rozanov, E., Winkel, L. H. E., Peter, T. and Stenke, A.: Improved tropospheric and stratospheric sulfur cycle in the aerosol–chemistry–climate model SOCOL-AERv2, *Geosc. Model Dev.*, 12, 3863-3887, <https://doi.org/10.5194/gmd-12-3863-2019>, 2019.
- 870 Ferek, R.J., Reid, J.S., Hobbs, P.V., Blake, D.R., and Liousse, C.: Emission factors of hydrocarbons, halocarbons, trace gases and particles from biomass burning in Brazil. *J. Geophys. Res. Atmos.*, 103, 32107-32118, <https://doi.org/10.1029/98jd00692>, 1998.
- 875 Fiedler, V., Arnold, F., Ludmann, S., Minikin, A., Hamburger, T., Pirjola, L., Dörnbrack, A., and Schlager, H.: African biomass burning plumes over the Atlantic: aircraft based measurements



- and implications for H<sub>2</sub>SO<sub>4</sub> and HNO<sub>3</sub> mediated smoke particle activation, *Atmos. Chem. Phys.*, 11, 3211–3225, <https://doi.org/10.5194/acp-11-3211-2011>, 2011.
- 880 Fountoukis, C. and Nenes, A.: ISORROPIA II: a computationally efficient thermodynamic equilibrium model for K–Ca–Mg–NH–Na–SO–NO–Cl–HO aerosols, *Atmos. Chem. Phys.*, 7, 4639–4659, 2007.
- Freiberg, J.: Conversion Limit And Characteristic Time of SO<sub>2</sub> Oxidation In Plumes, *Atmos. Environ.* 12, 339–347, 1978.
- 885 Fromm, M., Bevilacqua, R., Servranckx, R., Rosen, J., Thayer, J., Herman, J., and Larko, D.: Pyro-cumulonimbus injection of smoke to the stratosphere: Observations and impact of a super blowup in northwestern Canada on 3–4 August 1998, *J. Geophys. Res.*, 110, D08205, doi:10.1029/2004JD005350, 2005.
- 890 Fry, J. L., Draper, D. C., Zarzana, K. J., Campuzano-Jost, P., Day, D. A., Jimenez, J. L., Brown, S. S., Cohen, R. C., Kaser, L., Hansel, A., Cappellin, L., Karl, T., Hodzic Roux, A., Turnipseed, A., Cantrell, C., Lefer, B. L., and Grossberg, N.: Observations of gas- and aerosol-phase organic nitrates at BEACHON-RoMBAS 2011, *Atmos. Chem. Phys.*, 13, 8585–8605, 2013.
- 895 Guo, H., Weber, R. J., and Nenes, A.: High levels of ammonia do not raise fine particle pH sufficiently to yield nitrogen oxide-dominated sulfate production, *Scientific Reports*, 7(1), <https://doi.org/10.1038/s41598-017-11704-0>, 2017.
- 900 Guo, H., Xu, L., Bougiatioti, A., Cerully, K. M., Capps, S. L., Hite, J. R., Carlton, A. G., Lee, S.-H., Bergin, M. H., Ng, N. L., Nenes, A., and Weber, R. J.: Fine-particle water and pH in the southeastern United States, *Atmos. Chem. Phys.*, 15, 5211–5228, 2015.
- 905 Heim, E. W., Dibb, J., Scheuer, E., Jost, P. C., Nault, B. A., Jimenez, J. L., Peterson, D., Knote, C., Fenn, M., Hair, J., Beyersdorf, A. J., Corr, C., and Anderson, B. E.: Asian dust observed during KORUS-AQ facilitates the uptake and incorporation of soluble pollutants during transport to South Korea, *Atmos. Environ.*, 224, doi: 10.1016/j.atmosenv.2020.117305, 2020.
- 910 Hinckley, E.-L. S., Crawford, J. T., Fakhraei, H., and Driscoll, C. T.: A shift in sulfur-cycle manipulation from atmospheric emissions to agricultural additions, *Nat. Geosci.*, 13, 597–604, <https://doi.org/10.1038/s41561-020-0620-3>, 2020.
- 915 Hoesly, R. M., Smith, S. J., Feng, L., Klimont, Z., Janssens-Maenhout, G., Pitkanen, T., Seibert, J. J., Vu, L., Andres, R. J., Bolt, R. M., Bond, T. C., Dawidowski, L., Kholod, N., Kurokawa, J.-I., Li, M., Liu, L., Lu, Z., Moura, M. C. P., O'Rourke, P. R., and Zhang, Q.: Historical (1750–2014) anthropogenic emissions of reactive gases and aerosols from the Community Emissions Data System (CEDS), *Geosci. Model Dev.*, 11, 369–408, <https://doi.org/10.5194/gmd-11-369-2018>, 2018.



- 920 Keresztesi, A., Nita, I.-A., Boga, R., Birsan, M.-V., Bodor, Z., Szep, R.: Spatial and long-term analysis of rainwater chemistry over the conterminous United States, *Environ. Res.* 188, 109872, <https://doi.org/10.1016/j.envres.2020.109872>, 2020.
- 925 Koch, D., Jacob, D., Tegen, I., Rind, D., and Chin, M.: Tropospheric sulfur simulation and sulfate direct radiative forcing in the Goddard Institute for Space Studies general circulation model, *J. Geophys. Res.*, 104 (D19), 23,799–23,822, <https://doi.org/10.1029/1999JD900248>, 1999.
- 930 Kreidenweis, S. M., Petters, M. D., and De Mott, P. J.: Single-parameter estimates of aerosol water content, <https://doi.org/10.1088/1748-9326/3/3/035002>, 2008.
- 935 Lee, C., Martin, R. V., van Donkelaar, A., Lee, H., Dickerson, R. R., Hains, J. C., Krotkov, N., Richter, A., Vinnikov, K., and Schwab, J. J.: SO<sub>2</sub> emissions and lifetimes: Estimates from inverse modeling using in situ and global, space-based (SCIAMACHY and OMI) observations, *J. Geophys. Res.*, 116(D06304), 1–13, doi:10.1029/2010JD014758, 2011.
- 940 Lewis, K. A., Arnott, W. P., Moosmüller, H., Chakrabarty, R. K., Carrico, C. M., Kreidenweis, S. M., Day, D. E., Malm, W. C., Laskin, A., Jimenez, J. L., Ulbrich, I. M., Huffman, J. A., Onasch, T. B., Trimborn, A., Liu, L., and Mishchenko, M. I.: Reduction in biomass burning aerosol light absorption upon humidification: roles of inorganically-induced hygroscopicity, particle collapse, and photoacoustic heat and mass transfer, *Atmos. Chem. Phys.*, 9, 8949–8966, <https://doi.org/10.5194/acp-9-8949-2009>, 2009.
- 945 Liao, J., Wolfe, G. M., Hannun, R. A., St. Clair, J. M., Hanisco, T. F., Gilman, J. B., Lamplugh, A., Selimovic, V., Diskin, G. S., Nowak, J. B., Halliday, H. S., DiGangi, J. P., Hall, S. R., Ullmann, K., Holmes, C. D., Fite, C. H., Agastra, A., Ryerson, T. B., Peischl, J., Bourgeois, I., Warneke, C., Coggon, M. M., Gkatzelis, G. I., Sekimoto, K., Fried, A., Richter, D., Weibring, P., Apel, E. C., Hornbrook, R. S., Brown, S. S., Womack, C. C., Robinson, M. A., Washenfelder, R. A., Veres, P. R., and Neuman, J. A.: Formaldehyde evolution in US wildfire plumes during the Fire Influence on Regional to Global Environments and Air Quality experiment (FIREX-AQ), *Atmos. Chem. Phys.*, 21, 18319–18331, <https://doi.org/10.5194/acp-21-18319-2021>, 2021.
- 955 Lobert, J. M., Scharffe, D. H., Hao, W. M., Kuhlbusch, T. A., Seuwen, R., Warneck, P., and Crutzen, P. J.: Experimental evaluation of biomass burning emissions: Nitrogen and carbon containing compounds, in *Global Biomass Burning: Atmospheric, Climatic and Biospheric Implications*, edited by J. S. Levine, pp. 289–304, MIT Press, Cambridge, Mass., 1991.
- 960 Moch, J. M., Dovrou, E., Mickley, L. J., Keutsch, F. N., Cheng, Y., Jacob, D. J., Jiang, J., Li M., Munger, J. W., Qiao, X., and Zhang, Q.: Contribution of hydroxymethane sulfonate to ambient particulate matter: A potential explanation for high particulate sulfur during severe winter haze in Beijing. *Geophysical Research Letters*, 45, 11,969–11,979, <https://doi.org/10.1029/2018GL079309>, 2018.
- 965 Müller, M., Anderson, B. E., Beyersdorf, A. J., Crawford, J. H., Diskin, G. S., Eichler, P., Fried, A., Keutsch, F. N., Mikoviny, T., Thornhill, K. L., Walega, J. G., Weinheimer, A. J., Yang, M.,



- Yokelson, R. J., and Wisthaler, A.: In situ measurements and modeling of reactive trace gases in a small biomass burning plume, *Atmos. Chem. Phys.*, 16, 3813–3824, <https://doi.org/10.5194/acp-16-3813-2016>, 2016.
- 970 National Atmospheric Deposition Program (NRSP-3). NADP Program Office, Wisconsin State Laboratory of Hygiene, 465 Henry Mall, Madison, WI 53706, 2022.
- Nault, B. A., Campuzano-Jost, P., Day, D. A., Jo, D. S., Schorder, J. C., Allen, H. M., Bahreini, R., Bian, H., Blake, D. R., Chin, M., Clegg, S. L., Colarco, P. R., Crouse, J. D., Cubison, M. J.,  
975 DeCarlo, P. F., Dibb, J. E., Diskin, G. S., Hodzic, A., Hu, W., Katich, J. M., Kim, M. J., Kodros, J. K., Kupc, A., Lopez-Hilfiker, F. D., Marais, E. A., Middlebrook, A. M., Neuman, J. A., Nowak, J. B., Palm, B. B., Paulot, F., Pierce, J. R., Schill, G. P., Scheuer, E., Thornton, J. A., Tsigaridis, K., Wennberg, P. O., Williamson, C. J., and Jimenez J. L.: Chemical transport models often underestimate inorganic aerosol acidity in remote regions of the atmosphere. *Commun Earth Environ* 2, 93, <https://doi.org/10.1038/s43247-021-00164-0>, 2021.
- 980 Paatero, P. and Tapper, U.: Positive Matrix Factorization: a non-negative factor model with optimal utilization of error estimates of data values, 5, 111–126, <https://doi.org/10.1002/env.3170050203>, 1994.
- 985 Pandis, S. N., Wexler, A. S., and Seinfeld, J. H.: Dynamics of Tropospheric Aerosols, *J. Phys. Chem.*, 99 9646-9659, <https://doi.org/10.1021/j100024a003>, 1995.
- Pattantyus, A. K., Businger, S., and Howell, S. G.: Review of sulfur dioxide to sulfate aerosol chemistry at Kīlauea Volcano, Hawai‘I, *Atm. Env.*, 185, 262-271, <https://doi.org/10.1016/j.atmosenv.2018.04.055>, 2018.
- 990 Pham, M., J.-F. Muller, G. P. Brasseur, C. Granier, and G. Megie, A three-dimensional study of the tropospheric sulfur cycle, *J. Geophys. Res.*, 100, 26,061-26,092, <https://doi.org/10.1029/95JD02095>, 1995.
- 995 Qu, R. and Han, G.: A critical review of the variation in rainwater acidity in 24 Chinese cities during 1982–2018, *Elem. Sci. Anth.*, 9(1), <https://doi.org/10.1525/elementa.2021.00142>, 2021.
- 1000 Rickly, P. S., Xu, L., Crouse, J. D., Wennberg, P. O., and Rollins, A. W.: Improvements to a laser-induced fluorescence instrument for measuring SO<sub>2</sub> – impact on accuracy and precision, *Atmos. Meas. Tech.*, 14, 2429–2439, <https://doi.org/10.5194/amt-14-2429-2021>, 2021.
- 1005 Sachse, G. W., Jr, J. E. C., Hill, G. F., Wade, L. O., Burney, L. G., and Ritter, J. A.: Airborne tunable diode laser sensor for high-precision concentration and flux measurements of carbon monoxide and methane, in: *Measurement of Atmospheric Gases*, Measurement of Atmospheric Gases, 157–166, <https://doi.org/10.1117/12.46162>, 1991.
- Schueneman, M. K., Nault, B. A., Campuzano-Jost, P., Jo, D. S., Day, D. A., Schroder, J. C.,  
1010 Palm, B. B., Hodzic, A., Dibb, J. E., and Jimenez, J. L.: Aerosol pH indicator and organosulfate



- detectability from aerosol mass spectrometry measurements, *Atmos. Meas. Tech.*, 14, 2237–2260, <https://doi.org/10.5194/amt-14-2237-2021>, 2021.
- 1015 Seinfeld, J. H., and Pandis, S. N.: *Atmospheric Chemistry and Physics: From Air Pollution and Climate Change*, John Wiley, New York, 2006.
- 1020 Shao, J., Chen, Q., Wang, Y., Lu, X., He, P., Sun, Y., Shah, V., Martin, R. V., Philip, S., Song, S., Zhao, Y., Xie, Z., Zhang, L., and Alexander, B.: Heterogeneous sulfate aerosol formation mechanisms during wintertime Chinese haze events: air quality model assessment using observations of sulfate oxygen isotopes in Beijing, *Atmos. Chem. Phys.*, 19, 6107–6123, <https://doi.org/10.5194/acp-19-6107-2019>, 2019.
- 1025 Sinha, P., Hobbs, P. V., Yokelson, R. J., Bertschi, I. T., Blake, D. R., Simpson, I. J., Gao, S., Kirchstetter, T. W., and T. Novakov, T.: Emissions of trace gases and particles from savanna fires in southern Africa, *J. Geophys. Res.*, 108(D13), 8487, doi:10.1029/2002JD002325, 2003.
- 1030 Smith, S. J., van Aardenne, J., Klimont, Z., Andres, R. J., Volke, A., and Delgado Arias, S.: Anthropogenic sulfur dioxide emissions: 1850–2005, *Atmos. Chem. Phys.*, 11, 1101–1116, <https://doi.org/10.5194/acp-11-1101-2011>, 2011.
- 1035 Solberg, E. D., Malhi, S. S., Nyborg, M., Gill, K. S.: Fertilizer Type, Tillage, and Application Time Effects on Recovery of Sulfate-S from Elemental Sulfur Fertilizers in Fallow Field Soils, *Communications in Soil Science and Plant Analysis*, 34(5-6), 815–830, <https://doi.org/10.1081/CSS-120018977>, 2011.
- 1040 Song, S., Ma, T., Zhang, Y., Shen, L., Liu, P., Li, K., Zhai, S., Zheng, H., Gao, M., Moch, J. M., Duan, F., He, K., and McElroy, M. B.: Global modeling of heterogeneous hydroxymethanesulfonate chemistry, *Atmos. Chem. Phys.*, 21, 457–481, <https://doi.org/10.5194/acp-21-457-2021>, 2021.
- 1045 Sullivan, R. C., Boyer-Chelmo, H., Gorkowski, K., and Beydoun, H.: Aerosol Optical Tweezers Elucidate the Chemistry, Acidity, Phase Separations, and Morphology of Atmospheric Microdroplets, *Acc. Chem. Res.*, 53(11), 2498–2509, <https://doi.org/10.1021/acs.accounts.0c00407>, 2020.
- 1050 Susott, R. A., Olbu, G. J., Baker, S. P., Ward, D. E., Kauffmann, J. B., and Shea, R. W.: Carbon, hydrogen, nitrogen, and thermogravimetric analysis of tropical ecosystem biomass, in *Biomass Burning and Global Change*, vol. 1, edited by J. S. Levine, pp. 249 – 259, MIT Press, Cambridge, Mass., 1996.
- 1055 Tang, M. J., Telford, P. J., Pope, F. D., Rkiouak, L., Abraham, N. L., Archibald, A. T., Braesicke, P., Pyle, J. A., McGregor, J., Watson, I. M., Cox, R. A., and Kalberer, M.: Heterogeneous reaction of N<sub>2</sub>O<sub>5</sub> with airborne TiO<sub>2</sub> particles and its implication for stratospheric particle injection, *Atmos. Chem. Phys.*, 14, 6035–6048, <https://doi.org/10.5194/acp-14-6035-2014>, 2014.



- 1060 Ulbrich, I. M., Canagaratna, M. R., Zhang, Q., Worsnop, D. R., and Jimenez, J. L.: Interpretation of organic components from Positive Matrix Factorization of aerosol mass spectrometric data, *Atmos. Chem. Phys.*, 9, 2891–2918, 2009.
- U.S. Department of Agriculture: Crop Production 2019 Summary. By S. L. Censky and J. L. Parsons. January 2020. ISSN: 1057-7823, 2020.
- 1065 Vay, S. A., Tyler, S. C., Choi, Y., Blake, D. R., Blake, N. J., Sachse, G. W., Diskin, G. S., and Singh, H. B.: Sources and transport of  $\Delta^{14}\text{C}$  in  $\text{CO}_2$  within the Mexico City Basin and vicinity, *Atmos. Chem. Phys.*, 9, 4973–4985, <https://doi.org/10.5194/acp-9-4973-2009>, 2009.
- 1070 Wang, G., Zhang, R., Gomez, M. E., Yang, L., Zamora, M. L., Hu, M., Lin, Y., Peng, J., Guo, S., Meng, J., Li, J., Cheng, C., Hu, T., Ren, Y., Wang, Y., Gao, J., Cao, J., An, Z., Zhou, W., Li, G., Wang, J., Tian, P., Marrero-Ortiz, W., Secretst, J., Du, Z., Zheng, J., Shang, D., Zeng, L., Shao, M., Wang, W., Huang, Y., Wang, Y., Zhu, Y., Li, Y., Hu, J., Pan, B., Cai, L., Cheng, Y., Ji, Y., Zhang, F., Rosenfeld, D., Liss, P. S., Duce, R. A., Kolb, C. E., and Molina, M. J.: Persistent sulfate formation from London Fog to Chinese haze, *PNAS*, 113(48), 13630–13635, <https://doi.org/10.1073/pnas.1616540113>, 2016.
- 1075 Wang, Y., Zhang, Q. Q., Jiang, J., Zhou, W., Wang, B., He, K., Duan, F., Zhang, Q., Philip, S., and Xie, Y.: Enhanced sulfate formation during China's severe winter haze episode in January 2013 missing from current models, *J. Geophys. Res. Atmos.*, 119, 10,425–10,440, 2014, doi:10.1002/2013JD021426, 2014.
- 1080 Westerling, A. L., Hidalgo, H. G., Cayan, D. R., and Swetnam, T. W.: Warming and Earlier Spring Increase Western U.S. Forest Wildfire Activity, *Science*, 313(5789), 940–943, <https://doi.org/10.1126/science.1128834>, 2006.
- 1085 Wolfe, G. M., Marvin, M. R., Roberts, S. J., Travis, K. R., and Liao, J.: The framework for 0-D atmospheric modeling (F0AM) v3.1, *Geosci. Model Dev.*, 9(9), 3309–3319. DOI:10.5194/gmd-9-3309-2016, 2016.
- 1090 Yokelson, R. J., Griffith, D. W., and Ward, D. E.: Open-path Fourier transform infrared studies of large-scale laboratory biomass fires, *Geophys. Res. Atmos.*, 101(D15), 21067–21080, <https://doi.org/10.1029/96JD01800>, 1996.
- 1095 Zhang, Q., Zhou, S., Collier, S., Jaffe, D., Onasch, T., Shilling, J., Kleinman, L., and Sedlacek, A.: Understanding Composition, Formation, and Aging of Organic Aerosols in Wildfire Emissions via Combined Mountain Top and Airborne Measurements. ACS Symposium Series, 1299, Chapter 18, 363–385, <https://doi.org/10.1021/bk-2018-1299.ch018>, 2018.